AD_____

GRANT NUMBER DAMD17-96-1-6093

TITLE: An Overcomplete Enhancement of Digital Mammograms

PRINCIPAL INVESTIGATOR: Dr. Fred Taylor
Iztok Koren

CONTRACTING ORGANIZATION: University of Florida
Gainsville, FL 32611

REPORT DATE: August 1998

TYPE OF REPORT: Annual

PREPARED FOR: Commander
U.S. Army Medical Research and Materiel Command
Fort Detrick, Frederick, Maryland 21702-5012

DISTRIBUTION STATEMENT: Approved for public release;
distribution unlimited

The views, opinions and/or findings contained in this report are those of the author(s) and should not be construed as an official Department of the Army position, policy or decision unless so designated by other documentation.

**Reproduced From
Best Available Copy**

DTIC QUALITY INSPECTED 4

19981210 081

REPORT DOCUMENTATION PAGE

Form Approved
OMB No. 0704-0188

Public reporting burden for this collection of information is estimated to average 1 hour per response, including the time for reviewing instructions, searching existing data sources, gathering and maintaining the data needed, and completing and reviewing the collection of information. Send comments regarding this burden estimate or any other aspect of this collection of information, including suggestions for reducing this burden, to Washington Headquarters Services, Directorate for Information Operations and Reports, 1215 Jefferson Davis Highway, Suite 1204, Arlington, VA 22202-4302, and to the Office of Management and Budget, Paperwork Reduction Project (0704-0188), Washington, DC 20503.

1. AGENCY USE ONLY *(Leave blank)*	2. REPORT DATE	3. REPORT TYPE AND DATES COVERED
	August 1998	Annual (1 Aug 97 - 31 Jul 98)

4. TITLE AND SUBTITLE An Overcomplete Enhancement of Digital Mammograms

5. FUNDING NUMBERS
DAMD17-96-1-6093

6. AUTHOR(S)
Dr. Fred Taylor
Iztok Koren

7. PERFORMING ORGANIZATION NAME(S) AND ADDRESS(ES)
University of Florida
Gainesvill, FL 32611

8. PERFORMING ORGANIZATION REPORT NUMBER

9. SPONSORING/MONITORING AGENCY NAME(S) AND ADDRESS(ES)
Commander
U.S. Army Medical Research and Materiel Command
Fort Detrick, Frederick, Maryland 21702-5012

10. SPONSORING/MONITORING AGENCY REPORT NUMBER

11. SUPPLEMENTARY NOTES

12a. DISTRIBUTION / AVAILABILITY STATEMENT
Approved for public release; distribution unlimited

12b. DISTRIBUTION CODE

13. ABSTRACT *(Maximum 200*

This report describes our recent progress in the development of methodology for providing radiologists with a better viewing environment to facilitate the interpretation of mammograms. Our research has been targeting local enhancement of features of diagnostic importance and their fusion for an improved visualization in mammography.

After computing a multiscale directional derivative based wavelet decomposition, the transform coefficients are separately processed for enhancement of microcalcifications, circumscribed masses, and stellate lesions. The modified coefficients are then fused for reconstruction of an enhanced image with improved visibility of mammographic features. Both processing for enhancement of selected features and fusion of the resultant images are accomplished within a single wavelet transform framework, a fact which contributes to the computational efficiency of the derived method. The devised algorithm not only allows for efficient combination of specific features of importance in the contrast enhanced images, but also provides a flexible framework for incorporation of different enhancement methods and their independent optimization.

14. SUBJECT TERMS	15. NUMBER OF PAGES
Breast Cancer	34
	16. PRICE CODE

17. SECURITY CLASSIFICATION OF REPORT	18. SECURITY CLASSIFICATION OF THIS PAGE	19. SECURITY CLASSIFICATION OF ABSTRACT	20. LIMITATION OF ABSTRACT
Unclassified	Unclassified	Unclassified	Unlimited

FOREWORD

Opinions, interpretations, conclusions and recommendations are those of the author and are not necessarily endorsed by the U.S. Army.

____ Where copyrighted material is quoted, permission has been obtained to use such material.

____ Where material from documents designated for limited distribution is quoted, permission has been obtained to use the material.

____ Citations of commercial organizations and trade names in this report do not constitute an official Department of Army endorsement or approval of the products or services of these organizations.

____ In conducting research using animals, the investigator(s) adhered to the "Guide for the Care and Use of Laboratory Animals," prepared by the Committee on Care and Use of Laboratory Animals of the Institute of Laboratory Resources, National Research Council (NIH Publication No. 86-23, Revised 1985).

____ For the protection of human subjects, the investigator(s) adhered to policies of applicable Federal Law 45 CFR 46.

____ In conducting research utilizing recombinant DNA technology, the investigator(s) adhered to current guidelines promulgated by the National Institutes of Health.

____ In the conduct of research utilizing recombinant DNA, the investigator(s) adhered to the NIH Guidelines for Research Involving Recombinant DNA Molecules.

____ In the conduct of research involving hazardous organisms, the investigator(s) adhered to the CDC-NIH Guide for Biosafety in Microbiological and Biomedical Laboratories.

PI - Signature

9/15/88
Date

Table of Contents

List of Tables

List of Figures

1 Introduction

Breast cancer is the most frequently diagnosed malignancy among women in the United States [1]. In 1996, the American Cancer Society estimated that 184,300 women would be newly diagnosed with breast cancer and that 44,300 would die from the disease [1]. Breast cancer accounts for 31% of all cancers detected and 17% of all cancer deaths, and ranks as the second leading cause of death from cancer among women in the United States [1]. Five year survival rates are generally very high (93%) for breast cancer staged as being localized, falling to 72% for regional disease and only 18% for distant disease [2]. The early detection of breast cancer is clearly a key ingredient of any strategy designed to reduce breast cancer mortality.

Mammography's role is the early detection of breast cancer. Although more accurate than any other modality, existing techniques for mammography only find 80 to 90% of the breast cancers. Moreover, in 7 to 10% of cases, the cancer will not be visible on the mammogram. It has been suggested that mammograms as normally viewed, display only about 3% of the total information detected. Perception is a problem particularly for patients with dense fibroglandular patterns. The importance of diagnosis of breast cancer at an early stage is critical to patient survival. The general inability to detect small tumors and other salient features within mammograms motivates our investigation.

The goal of this project is to develop a diagnostic tool for radiologists that will refine the perception of mammographic features (including lesions, masses and calcifications) and improve the accuracy of diagnosis. Our research efforts are geared towards improving the local mammographic viewing environment by selectively processing mammograms for presence of different features, and towards providing a better global mammographic viewing environment by fusing together locally processed sections of images. By improving the visualization of breast pathology, we can increase the chances of early detection of breast cancers (improve quality) while requiring less time to evaluate mammograms for most patients (lower costs).

A major reason for poor visualization of small malignant masses is the subtle difference in x-ray attenuation between normal glandular tissues and malignant disease [3]. This fact makes the detection of small malignancies problematical, especially in younger women who have denser breast tissue. Although calcifications have high inherent attenuation properties, their small size also results in a low subject contrast [4]. As a result, the visibility of small tumors, and any associated microcalcifications, will always be a problem in mammography as it is currently performed using analog film.

We are investigating a methodology for accomplishing mammographic feature analysis

through multiscale representations. Wide variety of feature sizes and shapes in mammograms makes single-scale processing methods ineffective. In [5], it was shown that, in the context of mammography, multiscale image processing algorithms can outperform traditional contrast enhancement methods such as histogram equalization and unsharp masking. As reported in [6], an improvement in feature visualization was noted for mammograms processed using multiscale wavelet processing techniques. Furthermore, in [7], it was demonstrated that unsharp masking with a Gaussian lowpass filter can be formulated as a special case of contrast enhancement via a discrete dyadic wavelet transform.

Here, we present a scheme for local enhancement and fusion of clinically significant features. We devised a wavelet transform that is flexible enough for incorporation of a variety of enhancement methods and used the derived wavelet framework for enhancement of microcalcifications, circumscribed masses, and stellate lesions.

In the following sections, we briefly overview the contents of the report, list publications, and explain notation that we use.

1.1 Overview of Contents

Mammographic image enhancement methods are typically aimed at either improvement of the overall visibility of features or enhancement of a specific sign of malignancy. In this report, we present a synthesis of the two paradigms by means of image fusion. Section 2.1 introduces the idea and provides an overview of the algorithm.

Enhancement of different mammographic features is achieved within a single wavelet transform framework which must enable inclusion of a variety of methods (the derivations of such a versatile transform can be viewed as an extension of Task 3 of our Statement of Work). The transform is described in Section 2.2. First, Section 2.2.1 builds upon the foundation from our previous report to derive the transform, and then, Section 2.2.2 deals with fast implementations issues.

Different methods are used to enhance distinct mammographic features. Section 2.3 reports on three enhancement strategies. Enhancement of microcalcifications is based upon second derivatives of a Gaussian and given in Section 2.3.1. Circumscribed masses are enhanced through inputting the result from Laplacian of Gaussian approximations to enhancement functions as shown in Section 2.3.2. Stellate lesions are the topic of Section 2.3.3: directional derivatives are employed to determine local orientations needed for enhancement.

Lastly, Section 2.4 mentions the framework for fusion of enhanced features.

1.2 Publications

Below, we provide the list of publications accomplished during 1998.

[1] I. Koren, A. Laine, and F. Taylor, "Enhancement via fusion of mammographic features," in *Proc. IEEE Int. Conf. Image Process.*, Chicago, Il, Oct. 1998.

[2] I. Koren, A. Laine, S. Smith, E. Nickoloff, and F. Taylor, "Enhancement of mammograms via fusion of enhanced features," in *1st Int. Workshop on Computer-Aided Diagnosis*, Chicago, Il, Sep. 1998.

[3] I. Koren and A. Laine, "A discrete dyadic wavelet transform for multidimensional feature analysis," in M. Akay (Editor), *Time-Frequency and Wavelets in Biomedical Signal Engineering*, New York, NY: IEEE Press, 1998, pp. 425–449.

1.3 Notation

We use symbols $\boldsymbol{N}$, $\boldsymbol{Z}$, and $\boldsymbol{R}$ for the sets of naturals, integers, and reals, respectively. $L^2(\boldsymbol{R})$ and $L^2(\boldsymbol{R}^2)$ denote the Hilbert spaces of measurable, square-integrable functions $f(x)$ and $f(x,y)$, respectively.
The inner product of two functions $f(x) \in L^2(\boldsymbol{R})$ and $g(x) \in L^2(\boldsymbol{R})$ is given by

$$\langle f(x), g(x) \rangle = \int_{-\infty}^{\infty} f(x)\, g(x)\, dx.$$

The norm of a function $f(x) \in L^2(\boldsymbol{R})$ is defined as

$$\|f\| = \sqrt{\int_{-\infty}^{\infty} |f(x)|^2\, dx}.$$

The convolution of functions $f(x) \in L^2(\boldsymbol{R})$ and $g(x) \in L^2(\boldsymbol{R})$ is computed as

$$f * g(x) = \int_{-\infty}^{\infty} f(t)\, g(x-t)\, dt,$$

and the convolution of two functions $f(x,y) \in L^2(\boldsymbol{R}^2)$ and $g(x,y) \in L^2(\boldsymbol{R}^2)$ equals

$$f * g(x,y) = \int_{-\infty}^{\infty} \int_{-\infty}^{\infty} f(t_x, t_y)\, g(x-t_x, y-t_y)\, dt_x\, dt_y.$$

The Fourier transform of a function $f(x) \in L^2(\boldsymbol{R})$ is defined as

$$\hat{f}(\omega) = \int_{-\infty}^{\infty} f(x) e^{-j\omega x}\, dx,$$

and the Fourier transform of a function $f(x,y) \in L^2(\boldsymbol{R}^2)$ is equal to

$$\hat{f}(\omega_x, \omega_y) = \int_{-\infty}^{\infty} \int_{-\infty}^{\infty} f(x,y) e^{-j(\omega_x x + \omega_y y)}\, dx\, dy.$$

$l^2(\boldsymbol{Z})$ and $l^2(\boldsymbol{Z}^2)$ stand for the spaces of square-summable discrete signals $f(n)$ and $f(n_x, n_y)$, respectively.

The z-transform of a discrete signal $f(n) \in l^2(\boldsymbol{Z})$ is defined as

$$F(z) = \sum_{n=-\infty}^{\infty} f(n) z^{-n}.$$

The convolution of discrete signals $f(n) \in l^2(\boldsymbol{Z})$ and $g(n) \in l^2(\boldsymbol{Z})$ is equal to

$$f * g(n) = \sum_{m=-\infty}^{\infty} f(m)\, g(n-m),$$

and the convolution of discrete signals $f(n_x, n_y) \in l^2(\boldsymbol{Z}^2)$ and $g(n_x, n_y) \in l^2(\boldsymbol{Z}^2)$ is given by

$$f * g(n_x, n_y) = \sum_{m_x=-\infty}^{\infty} \sum_{m_y=-\infty}^{\infty} f(m_x, m_y)\, g(n_x - m_x, n_y - m_y).$$

The Fourier transform of a discrete signal $f(n) \in l^2(\boldsymbol{Z})$ is equal to the z-transform evaluated on the unit circle

$$F(\omega) = \sum_{n=-\infty}^{\infty} f(n) e^{-j\omega n},$$

and the Fourier transform of a discrete signal $f(n_x, n_y) \in l^2(\boldsymbol{Z}^2)$ is defined as

$$F(\omega_x, \omega_y) = \sum_{n_x=-\infty}^{\infty} \sum_{n_y=-\infty}^{\infty} f(n_x, n_y)\, e^{-j(\omega_x n_x + \omega_y n_y)}.$$

For later use, we define the following functions:

1. the unit impulse function
$$\delta_u(x) := \begin{cases} 1 & \text{for } x = 0 \\ 0 & \text{otherwise,} \end{cases}$$

2. the unit step function
$$u(x) := \begin{cases} 1 & \text{for } x \geq 0 \\ 0 & \text{for } x < 0, \end{cases}$$

3. the rectangular function
$$\text{rect}(x) := \begin{cases} 1 & \text{for } |x| \leq \frac{1}{2} \\ 0 & \text{for } |x| > \frac{1}{2}, \end{cases}$$

4. the sinc function
$$\text{sinc}(x) := \frac{\sin(\pi x)}{\pi x}, \quad \text{and}$$

5. the unit impulse sequence
$$\delta(n) := \begin{cases} 1 & \text{for } n = 0 \\ 0 & \text{otherwise,} \end{cases}$$

where $x \in \boldsymbol{R}$ and $n \in \boldsymbol{Z}$.

2 Body

2.1 Enhancement via Fusion

Existing methods of mammographic image enhancement can be divided roughly into two categories: (1) methods aimed at better visualization of all features present in the image [5, 10, 13, 14], and (2) methods that target specific features of importance (e.g., microcalcifications [15, 16], stellate lesions [9]).

Methods from the first category are not optimized for a specific type of cancer and frequently not even for mammography. Rather, they try to improve the perceptual quality of the entire image and are often developed with a framework more general than mammography alone in mind.

The second category methods concentrate on revelation of particular signs of malignancy. They can be very successful in their area of specialization; however, in order to process mammogram for presence of various features, one would need to apply different algorithms independently resulting in both larger number of images to be interpreted by a radiologist and increased computational complexity of such a procedure.

Here, we present an approach which overcomes these shortcomings and problematic limitations via synthesis of the two paradigms by means of image fusion.

The goal of our method is to adapt specific enhancement schemes for distinct mammographic features, and then combine the set of processed images into an enhanced image. The input mammographic image is first processed for enhancement of microcalcifications, masses, and stellate lesions. From the resulting enhanced images, the final enhanced image is synthesized by means of image fusion. Wavelet based image enhancement and fusion are merged into a unified framework, so that there is no need for carrying out the two operations independently (i.e., computing wavelet decompositions, modifying wavelet coefficients for enhancement of specific features, reconstructing the enhanced images, performing wavelet transforms of the enhanced images, fusing transform coefficients, and obtaining the final result by reconstruction from fused wavelet coefficients). Both enhancement and fusion are therefore implicit (i.e., performed in the wavelet domain only). Figure 1 presents a block scheme of the overall algorithm.

The algorithm consists of two major steps: (1) wavelet coefficients are modified distinctly for each type of malignancy; (2) the obtained multiple sets of wavelet coefficients are fused into a single set from which the reconstruction is computed. The devised scheme allows efficient deployment of an enhancement strategy appropriate for clinical screening protocols: enhancement algorithm is first developed for each specific type of feature independently, and the results are then combined using an appropriate fusion strategy.

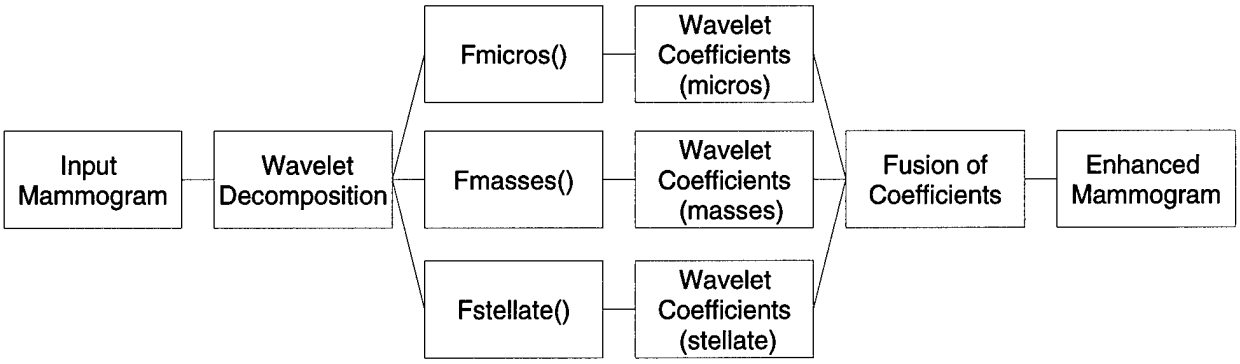

Figure 1: Overview of the algorithm.

The structure of the algorithm also enables independent development and optimization of enhancement strategies for individual mammographic features as well as the fusion module.

2.2 Wavelet Transform

In our previous report, we modified the one-dimensional discrete dyadic wavelet transform and used the obtained representation for derivation of several two-dimensional transforms. Here, we focus on approximations of steerable wavelets and employ the multiscale spline derivatives with both first and second derivative wavelet decomposition. Such a representation allows for both directional and isotropic processing of mammograms while being shift-invariant and aliasing-free as already reported. The derivation of the transform is presented in Section 2.2.1. As is the case with the majority of wavelet transforms, multiscale spline derivatives are implemented in a filter bank, so Section 2.2.2 deals with efficient implementations of the filters in the filter bank when the input image is mirror extended to alleviate boundary artifacts.

2.2.1 Multiscale Spline Derivatives

We define a steerable dyadic wavelet transform of a function $s(x,y) \in L^2(\boldsymbol{R}^2)$ at a scale 2^m, $m \in \boldsymbol{Z}$, as [9]

$$W^i_{2^m} s(x,y) = s * \psi^i_{2^m}(x,y), \tag{1}$$

where $\psi^i_{2^m}(x,y)$ denotes $\psi_{2^m}(x,y)$ rotated by θ_i, $\psi_{2^m}(x,y) = 2^{-2m}\psi(2^{-m}x, 2^{-m}y)$, $\psi(x,y)$ is a steerable wavelet that can be steered with I basis functions, and $\theta_i = \frac{i-1}{I}\pi$ with $i \in \{1,2,\ldots,I\}$. (For introduction to steerability, please refer to our previous report.) Analogous to the one-dimensional case, we require the two-dimensional Fourier plane to be covered by the dyadic dilations of $\hat{\psi}^i(2^m\omega_x, 2^m\omega_y)$: there must exist $A_3 > 0$ and $B_3 < \infty$

such that

$$A_3 \leq \sum_{m=-\infty}^{\infty} \sum_{i=1}^{I} |\hat{\psi}^i(2^m\omega_x, 2^m\omega_y)|^2 \leq B_3 \tag{2}$$

is satisfied almost everywhere.

If (nonunique) reconstructing functions $\chi^i_{2^m}(x,y)$ are chosen such that their Fourier transforms satisfy

$$\sum_{m=-\infty}^{\infty} \sum_{i=1}^{I} \hat{\psi}^i(2^m\omega_x, 2^m\omega_y)\, \hat{\chi}^i(2^m\omega_x, 2^m\omega_y) = 1, \tag{3}$$

the function $s(x,y)$ may be reconstructed from its steerable dyadic wavelet transform by

$$s(x,y) = \sum_{m=-\infty}^{\infty} \sum_{i=1}^{I} W^i_{2^m} s * \chi^i_{2^m}(x,y), \tag{4}$$

where $\chi^i_{2^m}(x,y)$ denotes $\chi_{2^m}(x,y)$ rotated by θ_i and $\chi_{2^m}(x,y) = 2^{-2m}\chi(2^{-m}x, 2^{-m}y)$.

We choose wavelets that are steerable analogs to the one-dimensional derivatives of central B-spline wavelets [18]:

$$\hat{\psi}(\omega_r, \omega_\theta) = (j\omega_r \cos(\omega_\theta))^d \left(\frac{\sin(\frac{\omega_r}{2})}{\frac{\omega_r}{2}} \right)^{p+d+1}, \tag{5}$$

where $\omega_r = \sqrt{\omega_x^2 + \omega_y^2}$, $\omega_\theta = \arg(\omega_x, \omega_y)$, and $d \in \{1,2\}$. These wavelets can be steered with $d+1$ basis functions.

Wavelets (5) are equal to d-th order derivatives of circularly symmetric spline functions in the direction of x-axis (note that knots for these splines are circles). To implement the transform efficiently, we approximate the wavelets with x-y separable wavelets

$$\psi(x,y) = \frac{d^d \beta_{p+d}(x)}{dx^d} \beta_{p+d}(y), \tag{6}$$

where $\beta_p(x)$ denotes the central B-spline of order p.

Based on the fact that B-splines tend to a Gaussian probability density function as their order increases, it is easy to see that both wavelets (5) and (6) converge to the same functions (i.e., d-th order derivatives of the normalized Gaussian in the direction of x-axis) as $p \to \infty$. In order to steer wavelets $\psi(x,y)$ given by (6) (note that steering will be only approximate, since these wavelets are not steerable), we need to find basis functions that will approximately steer $\psi(x,y)$. To accomplish this, we take advantage of the property of circularly symmetric functions that rotations of their directional derivatives are equal to directional derivatives in rotated directions:

$$\mathcal{R}_{\theta_0} \left\{ \frac{\partial^d \varrho_c(x,y)}{\partial \vec{n}^d} \right\} = \frac{\partial^d \varrho_c(x,y)}{\partial \vec{n}^d_{\theta_0}},$$

where $\mathcal{R}_{\theta_0}$ stands for rotation by θ_0, $\frac{\partial \varrho_c(x,y)}{\partial \vec{n}} = \vec{n}\,\vec{\nabla}\varrho_c(x,y)$, $\varrho_c(x,y)$ is a circularly symmetric function, and $\vec{n}_{\theta_0}$ denotes vector $\vec{n} = (\cos\theta, \sin\theta)$ rotated by θ_0.
Let us choose

$$\varrho(x,y) = \beta_{p+d}(x)\beta_{p+d}(y),$$

which is approximately circularly symmetric function for higher order splines. A rotation of $\psi(x,y) = \frac{\partial^d \varrho(x,y)}{\partial x^d}$ from Equation (6) by θ_0 can therefore be approximated by

$$\psi^{\theta_0}(x,y) \simeq \frac{\partial^d \varrho(x,y)}{\partial \vec{n}^d} = \sum_{i=0}^{d} \binom{d}{i} n_x^{d-i} n_y^i \frac{d^{d-i}\beta_{p+d}(x)}{dx^{d-i}} \frac{d^i \beta_{p+d}(y)}{dy^i}, \tag{7}$$

where $\vec{n} = (\cos\theta_0, \sin\theta_0) = (n_x, n_y)$. (Note that in case of Gaussian, which is both x-y separable and circularly symmetric, Equation (7) becomes exact.)
To derive an algorithm for the fast computation of the transform, we introduce two smoothing functions such that

$$\hat{\phi}(\omega_x,\omega_y)\,\hat{\varphi}(\omega_x,\omega_y) = \sum_{m=0}^{\infty}\sum_{i=1}^{I} \hat{\psi}^i(2^m\omega_x, 2^m\omega_y)\,\hat{\chi}^i(2^m\omega_x, 2^m\omega_y). \tag{8}$$

Using a set of basis functions (7) that approximately steer wavelets (6), we want to construct a transform such that Equations (1) through (4)and (8) will be valid (superscript i must be viewed now as an index, rather than rotation by θ_i).
Let $F(\omega)$ be a digital filter frequency response and let us denote

$$F_s(\omega) = e^{j\omega s} F(\omega)$$

with s being a filter dependent sampling shift needed to obtain finite impulse response (FIR) filters.
In frequency domain, we can express basis functions from (7) as

$$\hat{\psi}^{i+1}(\omega_x,\omega_y) = G_{-s}^{d-i}(\omega_x) G_{-s}^{i}(\omega_y) \hat{\beta}_{p+i}(\omega_x)\hat{\beta}_{p+d-i}(\omega_y), \qquad i \in \{0,1,2\}, \tag{9}$$

where $G^d(\omega)$ is given by

$$G^d(\omega) = e^{j\omega s}\left(2j\sin\left(\frac{\omega}{2}\right)\right)^d, \tag{10}$$

where d is the order of the derivative, $d \in \{1,2\}$, the sampling shift for filter (10) is $s = \frac{d \bmod 2}{2}$, and $G^0(\omega) = 1$.
Since we are interested in the first and second derivative wavelets, we impose

$$\hat{\varphi}(\omega_x,\omega_y) = \hat{\phi}(\omega_x,\omega_y) = \hat{\beta}_p(\omega_x)\hat{\beta}_p(\omega_y)$$

and choose

$$\hat{\chi}^1(\omega_x,\omega_y) = K_s^2(\omega_x)T(\omega_y)\hat{\beta}_p(\omega_x)\hat{\beta}_{p-2}(\omega_y), \tag{11}$$

$$\hat{\chi}^2(\omega_x,\omega_y) = K_s^1(\omega_x)K_s^1(\omega_y)\hat{\beta}_{p-1}(\omega_x)\hat{\beta}_{p-1}(\omega_y), \tag{12}$$

$$\hat{\chi}^3(\omega_x,\omega_y) = T(\omega_x)K_s^2(\omega_y)\hat{\beta}_{p-2}(\omega_x)\hat{\beta}_p(\omega_y), \tag{13}$$

where

$$K^d(\omega) = \frac{1}{(2j)^d}\left(e^{-j\omega s}\sin\left(\frac{\omega}{2}\right)\right)^{d \bmod 2}\left(\sum_{m=0}^{p}\left(\cos\left(\frac{\omega}{2}\right)\right)^{2m}\right)^{\lfloor\frac{d+1}{2}\rfloor}, \tag{14}$$

with the sampling shift for $K^d(\omega)$ being the same as the one for $G^d(\omega)$, and

$$T(\omega) = |H(\omega)|^2 \tag{15}$$

with

$$H(\omega) = e^{j\omega s}\left(\cos\left(\frac{\omega}{2}\right)\right)^{p+1}, \tag{16}$$

the sampling shift for $H(\omega)$ being $s = \frac{(p+1) \bmod 2}{2}$.
Using the relation derived in the previous report

$$\hat{\beta}_p(2\omega) = H_{-s}(\omega)\hat{\beta}_p(\omega) \tag{17}$$

together with Equations (9) and (11) through (13) with Equation (8) results in

$$G^2(\omega_x)K^2(\omega_x)T(\omega_y) + G^1(\omega_x)K^1(\omega_x)G^1(\omega_y)K^1(\omega_y) + T(\omega_x)G^2(\omega_y)K^2(\omega_y) + \\ + |H(\omega_x)H(\omega_y)|^2 = 1.$$

Next, we derive a filter bank implementation of the transform. Assuming a bandlimited input signal $\hat{s}(\omega_x,\omega_y) = 0$ for $|\omega_x| > \pi$ or $|\omega_y| > \pi$ and using Shannon's sampling theorem in two dimensions [19] with Equation (1) and basis functions from Equation (9), we can write

$$W_1^i s(x,y) = \int_{-\infty}^{\infty}\int_{-\infty}^{\infty}\sum_{i_x=-\infty}^{\infty}\sum_{i_y=-\infty}^{\infty} s(i_x,i_y)\,\mathrm{sinc}(t_x - i_x)\,\mathrm{sinc}(t_y - i_y)\cdot$$

$$\cdot \sum_{m_x=-\infty}^{\infty} g_{-s}^{d-i}(m_x)\beta_{p+i}(x - t_x - m_x)\sum_{m_y=-\infty}^{\infty} g_{-s}^{i}(m_y)\beta_{p+d-i}(y - t_y - m_y)\,dt_x\,dt_y,$$

where $i \in \{0,1,2\}$ as in Equation (9).
We approximate sinc functions with r-order cardinal splines, then use the relation between cardinal and B-splines

$$\eta_r(x) = \sum_{i=-\infty}^{\infty} b_r^{-1}(i)\beta_r(x - i)$$

Table 1: Transfer functions of direct B-spline filters for orders from 0 to 9.

p	$B_p^{-1}(z)$
0	1
1	1
2	$\frac{8}{z+6+z^{-1}}$
3	$\frac{6}{z+4+z^{-1}}$
4	$\frac{384}{z^2+76z+230+76z^{-1}+z^{-2}}$
5	$\frac{120}{z^2+26z+66+26z^{-1}+z^{-2}}$
6	$\frac{46080}{z^3+722z^2+10543z+23548+10543z^{-1}+722z^{-2}+z^{-3}}$
7	$\frac{5040}{z^3+120z^2+1191z+2416+1191z^{-1}+120z^{-2}+z^{-3}}$
8	$\frac{10321920}{z^4+6552z^3+331612z^2+2485288z+4675014+2485288z^{-1}+331612z^{-2}+6552z^{-3}+z^{-4}}$
9	$\frac{362880}{z^4+502z^3+14608z^2+88234z+156190+88234z^{-1}+14608z^{-2}+502z^{-3}+z^{-4}}$

and get

$$\mathcal{F}\{W_{2^m}^i s(x,y)\Big|_{x=n_x,y=n_y}\} \simeq S(\omega_x,\omega_y)\, B_r^{-1}(\omega_x)\, B_r^{-1}(\omega_y)\, B_{p+r+i+1}(\omega_x)\cdot$$
$$\cdot B_{p+r+d-i+1}(\omega_y)\, G_{-s}^{d-i}(2^m\omega_x)\, G_{-s}^{i}(2^m\omega_y) \prod_{n=0}^{m-1} H_{-s}^{p+i}(2^n\omega_x) H_{-s}^{p+d-i}(2^n\omega_y), \qquad (18)$$

where $B_p^{-1}(\omega)$ denotes the Fourier transform of the direct B-spline filter of order p. Table 1 shows the z-transforms of direct B-spline filters for the first ten orders.

Using Equation (18) with an approximation $B_{p+r+i+1}(\omega) \simeq B_{p+r}(\omega)B_i(\omega)$, we can obtain a filter bank implementation of the transform decomposition. The reconstruction part follows from Equations (8), (9), and (11) through (13). Figure 2 shows a filter bank implementation of the transform. Noninteger shifts at scale 1 are rounded to the nearest integer. Tables 2 through 5 list impulse responses of the filters used in the filter bank for $p \in \{0,1,2\}$.

The derived transform enables both second derivative directional analysis and Laplacian of Gaussian approximations across dyadic scales (the latter can be obtained through summation of the outputs from blocks $G^2(2^m\omega)$ applied along x and y axis). Furthermore, addition of a block $G_{-s}^1(2^m\omega)$ at each level of decomposition allows first derivative

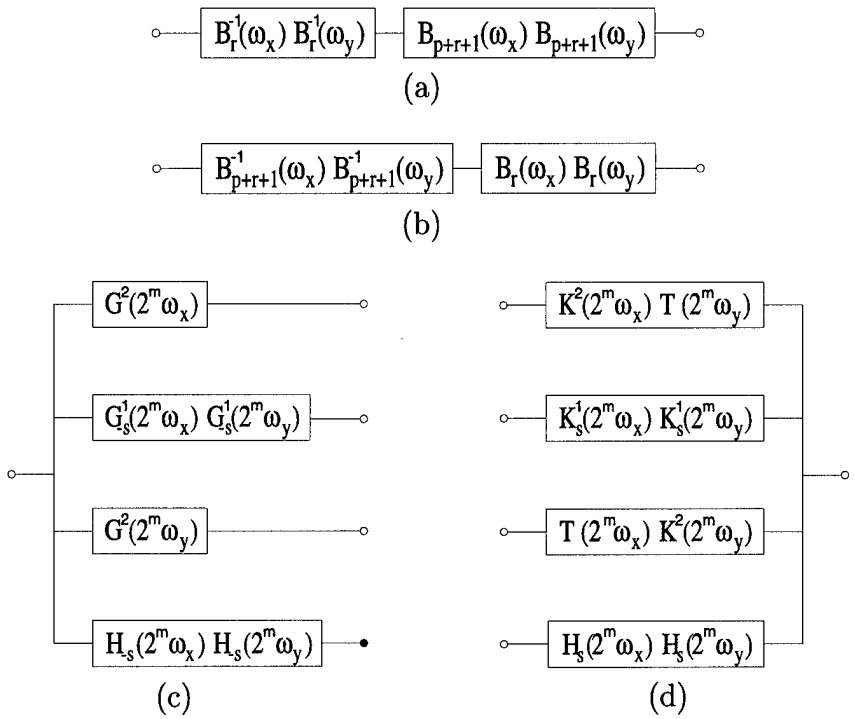

Figure 2: Filter bank implementation of multiscale spline derivatives for $m \in [0, M-1]$: (a) Prefiltering, (b) postfiltering, (c) decomposition module, and (d) reconstruction module.

Table 2: Impulse responses $g^1(n)$ and $g^2(n)$.

n	$g^1(n)$	$g^2(n)$
-1	1	1
0	-1	-2
1		1

Table 3: Impulse responses $h(n)$, $k^1(n)$, $k^2(n)$, and $t(n)$ for p=0.

n	$h(n)$	$k^1(n)$	$k^2(n)$	$t(n)$
-1	0.5			0.25
0	0.5	-0.25	-0.25	0.5
1		0.25		0.25

Table 4: Impulse responses $h(n)$, $k^1(n)$, $k^2(n)$, and $t(n)$ for p=1.

n	$h(n)$	$k^1(n)$	$k^2(n)$	$t(n)$
-2				0.0625
-1	0.25	-0.0625	-0.0625	0.25
0	0.5	-0.3125	-0.375	0.375
1	0.25	0.3125	-0.0625	0.25
2		0.0625		0.0625

Table 5: Impulse responses $h(n)$, $k^1(n)$, $k^2(n)$, and $t(n)$ for p=2.

n	$h(n)$	$k^1(n)$	$k^2(n)$	$t(n)$
-3				0.015625
-2	0.125	-0.015625	-0.015625	0.09375
-1	0.375	-0.109375	-0.125	0.234375
0	0.375	-0.34375	-0.46875	0.3125
1	0.125	0.34375	-0.125	0.234375
2		0.109375	-0.015625	0.09375
3		0.015625		0.015625

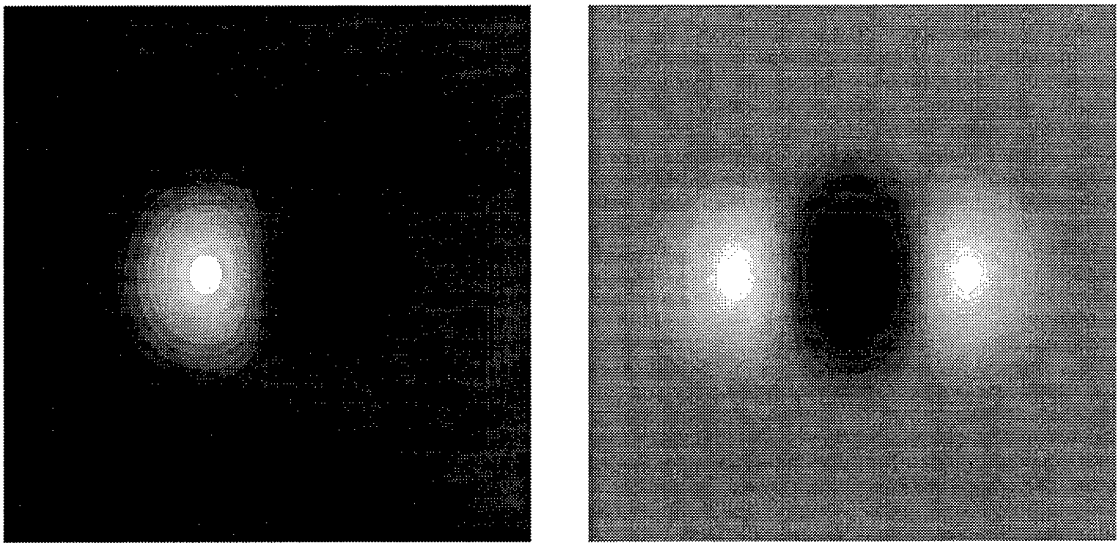

(a) (b)

Figure 3: Spline derivatives in the x-axis direction. (a) Wavelet equal to the first derivative of a quartic spline. (b) Wavelet equal to the second derivative of a quintic spline.

directional analysis as well. Figure 3 shows first and second derivative wavelets obtained as linear combinations of cubic B-splines.

2.2.2 Filter Implementations

Since all two-dimensional filters used in the filter bank implementation of the transforms are x-y separable, only one-dimensional filters need to be implemented. We describe the implementation of finite impulse response (FIR) filters first and then treat prefiltering and postfiltering infinite impulse response (IIR) filters from Figure 2(a) and (b).
Let us refer to filters applied at scale 2^m as filters at level m+1, and let filters at level 1 (Equations (10), (14), (15), and (16) be called "original filters," to distinguish them from their upsampled versions. Let us split the input to the filter bank from Figure 2 into image matrix rows and columns, each corresponding to a real signal $s(n) \in l^2(\boldsymbol{Z})$, $n \in [0, N-1]$.

Depending on the length of each filter impulse response, filtering an input signal may be computed either by multiplying the discrete Fourier transforms of the two sequences or by circularly convolving $s(n)$ with a filter's impulse response. Using circular rather than linear convolution, as is customary in image processing, can lead to boundary artifacts caused by abrupt changes in the periodically extended signal. A common remedy for such a problem is realized by constructing a mirror extended signal [12]

$$s_{me}(n) = \begin{cases} s(-n-1) & \text{if } n \in [-N, -1] \\ s(n) & \text{if } n \in [0, N-1], \end{cases} \tag{19}$$

where we chose the signal $s_{me}(n)$ to be supported in $[-N, N-1]$.
Let us classify symmetric/antisymmetric real even-length signals into four types [20]:

Type I $f(n) = f(-n)$,

Type II $f(n) = f(-n-1)$,

Type III $f(n) = -f(-n)$,

Type IV $f(n) = -f(-n-1)$,

where $n \in [-N, N-1]$. Note that for Type I signals the values at $f(0)$ and $f(-N)$ are unique, and that for Type III signals the values at $f(0)$ and $f(-N)$ are equal to zero. (This is important for storage requirements: for signals of Type II or Type IV, N samples need to be saved, while Type I and Type III signals require $N+1$ and $N-1$ sample representations, respectively.)
Using properties of the Fourier transform, it is easy to show that the convolution of symmetric/antisymmetric real signals results in a symmetric/antisymmetric real signal. If a symmetric/antisymmetric real signal has an even length, then there always exists an integer shift such that the shifted signal belongs to one of the above types.
Now, we are ready to examine the filter bank implementation of the wavelet transform from Figure 2 with filters given by Equations (10), (14), (15), and (16) driven by mirrored signals of the form $s_{me}(n)$ from Equation (19) at the input. Let the number of levels M be restricted by

$$M \leq 1 + \log_2 \frac{N-1}{L_{max}-1}, \tag{20}$$

where L_{max} is the length of the longest original FIR filter impulse response.
Each FIR filter block in the filter bank consists of a filter and a circular shift operator. Equation (20) guarantees that the length of the filter impulse response does not exceed the length of the signal at any block.

Since our mirror extended input row or column $s_{me}(n)$ is of Type II and noninteger shifts at level 1 are rounded to the nearest integer, it follows that a processed one-dimensional signal at any point in the filter bank belongs to one of the types defined above. This means that filtering a signal of length $2N$ can be reduced to filtering a signal of approximately one half of its length.

Implementation is particularly simple for FIR filters designed with $d=2$ and p odd. Filters are of Type I in this case, so their output will be of Type II. An FIR filter block from the filter bank shown in Figure 2 can therefore be implemented by

$$F_{s,m}u(n) = f(0)u_{II}(n) + \sum_{i=1}^{\frac{L-1}{2}} f(i)[u_{II}(n-2^m i) + u_{II}(n+2^m i)], \qquad n \in [0, N-1], \tag{21}$$

where

$$u_{II}(n) = \begin{cases} u(-n-1) & \text{if } n \in [-\frac{N}{2}, -1] \\ u(n) & \text{if } n \in [0, N-1] \\ u(2N-n-1) & \text{if } n \in [N, \frac{3N}{2}], \end{cases} \tag{22}$$

$u(n)$ is an input signal to a block, $f(n)$ is an impulse response of $G^2(2^m\omega)$, $K^2(2^m\omega)$, $T(2^m\omega)$, or $H(2^m\omega)$ with p odd, L is the length of the filter, and N is the length of an input signal $s(n)$ to the filter bank. Implementation of filters $b_p(n)$ used for prefiltering and postfiltering (Figure 2(a) and (b)) represents a special case of Equation (21) with $m=0$.

A filter bank with the above implementation of blocks and signal $s(n)$ at the input yields equivalent results as circular convolution of input $s_{me}(n)$ as defined by Equation (19). In addition to requiring one half the amount of memory, the computational savings over a circular convolution implementation of blocks are, depending on the original filter length, three to four times fewer multiplications and one half as many additions.

A similar approach is used for other filters. The problem becomes slightly more involved in this case, because the filters change type from first to subsequent levels, and the signal component type can be altered by a filter block as well. As a consequence, an implementation of blocks that use distinct original filters may not be the same, and the implementation of blocks at level 1 may differ from the implementation of blocks at other levels of analysis.

The decomposition blocks at level 1 can be implemented by

$$G^1_{-s,0}u(n) = \sum_{i=0}^{\frac{L}{2}-1} g(i)[u_{II}(n-i-1) - u_{II}(n+i)], \qquad n \in [1, N-1]$$

and

$$H_{-s,0}u(n) = \sum_{i=0}^{\frac{L}{2}-1} h(i)[u_{II}(n-i-1) + u_{II}(n+i)], \qquad n \in [0, N],$$

for p even, where $u_{II}(l)$ is defined by (22), $g(n)$ and $h(n)$ are impulse responses of the filters computed from (10) and (16), respectively, and L is the length of the corresponding impulse response.

The output from a block $G^1_{-s}(\omega)$ at level 1 is of Type III, while the output from $H_{-s}(\omega)$ at the same level is of Type I.

The decomposition blocks at subsequent levels $m \in [1, M-1]$ can be implemented by

$$G^1_{-s,m}u(n) = \sum_{i=0}^{\frac{L}{2}-1} g(i)[u_I(n-2^m(i+s)) - u_I(n+2^m(i+s))], \qquad n \in [1, N-1],$$

for p even,

$$G^1_{-s,m}u(n) = \sum_{i=0}^{\frac{L}{2}-1} g(i)[u_{II}(n-2^m(i+s)) - u_{II}(n+2^m(i+s))], \qquad n \in [0, N-1],$$

for p odd,

$$F_{-s,m}u(n) = f(0)u_I(n) + \sum_{i=1}^{\frac{L-1}{2}} f(i)[u_I(n-2^m i) + u_I(n+2^m i)], \qquad n \in [0, N], \tag{23}$$

with $f(n) = g(n)$ for $d{=}2$ and p even,

$$H_{-s,m}u(n) = \sum_{i=0}^{\frac{L}{2}-1} h(i)[u_I(n-2^m(i+s)) + u_I(n+2^m(i+s))], \qquad n \in [0, N], \tag{24}$$

for p even, where

$$u_I(n) = \begin{cases} u(-n) & \text{if } n \in [-\frac{N}{2}, -1] \\ u(n) & \text{if } n \in [0, N] \\ u(2N-n) & \text{if } n \in [N+1, \frac{3N}{2}]. \end{cases} \tag{25}$$

The outputs from blocks $G_{-s}(2^m\omega)$ are of Type III for $d{=}1$ and p even, of Type IV for $d{=}1$ and p odd, and of Type I for $d{=}2$ and p even, whereas the outputs from $H_{-s}(2^m\omega)$ are of Type I for p even.

Next, the reconstruction blocks at level 1 can be implemented by

$$K^1_{s,0}u(n) = \sum_{i=1}^{\frac{L}{2}} k(i)[u_{III}(n-i+1) - u_{III}(n+i)], \qquad n \in [0, N-1]$$

and

$$H_{s,0}u(n) = \sum_{i=1}^{\frac{L}{2}} h(i)[u_I(n-i+1) + u_I(n+i)], \qquad n \in [0, N-1],$$

for p even, where

$$u_{III}(n) = \begin{cases} -u(-n) & \text{if } n \in [-\frac{N}{2}, -1] \\ 0 & \text{if } n = 0 \\ u(n) & \text{if } n \in [1, N-1] \\ 0 & \text{if } n = N \\ -u(2N-n) & \text{if } n \in [N+1, \frac{3N}{2}], \end{cases} \tag{26}$$

$u_I(n)$ is as defined by (25) and $k(n)$ is an impulse response of the filter from (14). Note that both outputs from blocks $K_s^1(\omega)$ and $H_s(\omega)$ are of Type II.

The reconstruction blocks at subsequent levels can be implemented by

$$K_{s,m}^d u(n) = \sum_{i=0}^{\frac{L}{2}-1} k(i+1)[u_{III}(n-2^m(i+s)) - u_{III}(n+2^m(i+s))], \qquad n \in [0, N],$$

for d=1 and p even, (23) with $f(n) = k(n)$ for d=2 and p even,

$$K_{s,m}^d u(n) = \sum_{i=0}^{\frac{L}{2}-1} k(i+1)[u_{IV}(n-2^m(i+s)) - u_{IV}(n+2^m(i+s))], \qquad n \in [0, N-1],$$

for d=1 and p odd,

$$H_{s,m} u(n) = H_{-s,m} u(n),$$

for p even, where $u_{III}(l)$ is given by (26),

$$u_{IV}(n) = \begin{cases} -u(-n-1) & \text{if } n \in [-\frac{N}{2}, -1] \\ u(n) & \text{if } n \in [0, N-1] \\ -u(2N-n-1) & \text{if } n \in [N, \frac{3N}{2}], \end{cases}$$

and $H_{-s,m}u(n)$ is specified by Equation (24). We observe that the outputs from blocks $K_s^d(2^m\omega)$ and $H_s(2^m\omega)$, $m \in [1, M-1]$, for p even are of Type I.

When we compare the above implementation of blocks to circular convolution driven by a mirrored signal $s_{me}(n)$ at the input, we observe that approximately twofold less memory space, three to four times fewer multiplications and one half as many additions are required. (For Type I signals an additional sample has to be stored because two values are without a pair).

The implementation presented in this section performs all operations in the spatial domain; however, one could also implement the structures shown in Figure 2 with an input signal $s_{me}(n)$ in the frequency domain. For short filter impulse responses, such as those given in Tables 3, 4 and 5, the spatial implementation described in this section is certainly more efficient. For long filter impulse responses, however, filtering is faster if implemented in the frequency domain. Additional details on alternative FIR filter implementation strategies can be found in [21].

Implementation of IIR filters $b_p^{-1}(n)$ used for prefiltering and postfiltering is a bit more involved than the one of their FIR counterparts. Fortunately, the number of different cases is much smaller here: possible input to $b_p^{-1}(n)$ in the filter bank from Figure 2 is either of Type II or of Type I (symmetry types for IIR filters slightly differ from those defined for FIR filters: here, mirror extended signals are periodically repeated, so that they stretch from $-\infty$ to ∞). We use ideas and a few results from [22].

Let us first take a closer look at the system function $B_p^{-1}(z)$ with $p \in \{2, 3\}$. This function can be written as a cascade of terms

$$E(z) = \frac{1}{z - \frac{1+\alpha^2}{\alpha} + z^{-1}} = \frac{-\alpha}{(1-\alpha z^{-1})(1-\alpha z)}, \tag{27}$$

which can be expressed in a parallel form as

$$E(z) = \frac{-\alpha}{1-\alpha^2}\left(\frac{1}{1-\alpha z^{-1}} + \frac{1}{1-\alpha z} - 1\right), \tag{28}$$

where α and $\frac{1}{\alpha}$ are poles of the causal and the anticausal filter, respectively.

The impulse response of this term can be written as

$$e(n) = \frac{-\alpha}{1-\alpha^2}\alpha^{|n|}.$$

We choose to implement $E(z)$ in a cascade form and therefore extract the difference equations from Equation (27):

$$c^+(n) = u(n) + \alpha\, c^+(n-1) \qquad n = 1, 2, \ldots, N-1, \tag{29}$$

and

$$c(n) = \alpha\,(c(n+1) - c^+(n)) \qquad n = N-2, N-3, \ldots, 0, \tag{30}$$

where $u(n)$ denotes the input to the block, $c^+(n)$ is the output from the causal part, and $c(n)$ stands for the output from the block.

To solve Equations (29) and (30) we need boundary conditions $c^+(0)$ and $c(N-1)$. We derive

$$c^+(0) = \sum_{i=-\infty}^{0} \alpha^{-i} u_{IIp}(i) = u(0) + \sum_{i=0}^{N-1} \frac{\alpha^{i+1} + \alpha^{2N-i}}{1-\alpha^{2N}} u(i) \simeq u(0) + \sum_{i=0}^{i_0} \alpha^{i+1} u(i), \tag{31}$$

and, using parallel form (28)

$$\begin{aligned} c(N-1) &= \frac{-\alpha}{1-\alpha^2}(c^+(N-1) + \sum_{i=0}^{N-1} \frac{\alpha^{N-i} + \alpha^{N+1+i}}{1-\alpha^{2N}} u(i)) \simeq \\ &\simeq \frac{-\alpha}{1-\alpha^2}(c^+(N-1) + \sum_{i=N-1-i_0}^{N-1} \alpha^{N-i} u(i)), \end{aligned} \tag{32}$$

where

$$u_{IIp}(n) = \begin{cases} u_{II}(n \bmod (2N)) & \text{if } n \geq 0 \\ u_{II}(-(n+1) \bmod (2N)) & \text{if } n < 0, \end{cases}$$

$$u_{II}(n) = \begin{cases} u(n) & \text{if } n \in [0, N-1] \\ u(2N-n-1) & \text{if } n \in [N, 2N-1], \end{cases}$$

N is the length of an input signal to the filter bank, and $i_0 < N-1$ is selected such that α^{i_0} falls below a predefined precision threshold.

For orders p greater than three, we implement $B_p^{-1}(z)$ as a cascade of terms $E(z)$ with different α's. Note that the output from block $E(z)$ is always of the same type as the input to it.

2.3 Enhancement of Mammographic Features

2.3.1 Microcalcifications

Microcalcifications appear on mammograms in approximately half of breast cancer cases. The assessment of shape, number, and distribution of microcalcifications is important for a radiologist to reach the correct diagnosis. Microcalcifications are smaller than 1 mm in size and can be difficult to locate when they are superimposed on dense breast tissue.

Several techniques have been developed to improve the visibility of microcalcifications [15, 16, 23, 24]. The approach devised by Strickland and Hahn [15] is particularly well suited for our framework: they used an undecimated wavelet transform to approximate second derivatives of a Gaussian probability density function for a multiscale matched filtering for presence of microcalcifications.

Strickland and Hahn based their method on the observation that the average microcalcification can be modeled by a circularly symmetric Gaussian function. Using a combination of a separable Markov process with autocorrelation $r_{nn} = \sigma_n^2 e^{-\alpha\sqrt{|k|+|l|}}$ and a nonseparable Markov process with autocorrelation $r_{nn} = \sigma_n^2 e^{-\alpha\sqrt{k^2+l^2}}$ to represent mammogram texture, they obtained the separable matched filter

$$M_{sep}(\omega_x, \omega_y) = M(\omega_x)M(\omega_y), \tag{33}$$

where

$$M(\omega) \simeq \frac{\sigma\sqrt{\pi}\omega^2}{\sqrt{2}\alpha\sigma_n} e^{\frac{\sigma^2\omega^2}{2}},$$

and the nonseparable matched filter

$$M_{nsep}(\omega_x, \omega_y) \simeq \frac{\pi\sigma^2}{\sigma_n^2}(\omega_x^2 + \omega_y^2) e^{\frac{\sigma^2\omega^2}{2}}. \tag{34}$$

In order to deal with different sizes of microcalcifications, one must vary σ of matched filters (33) and (34) appropriately. In Strickland and Hahn's scheme, a wavelet decomposition was chosen to approximate the matched filters across the desired scale range. Considering the 100μm resolution of the Nijmegen database, the wavelet transform was computed over the first 4 octaves. For a denser sampling of scale, voices were inserted at octaves "2.5" and "3.5." The wavelet analysis stage acted as a bank of matched filters; wavelet coefficients at locations indicating microcalcifications were multiplied by a gain factor, and then the inverse wavelet transform was applied to the modified coefficients.
In our approach, microcalcifications are modeled by central B-splines. Using the relation between the standard deviation of a Gaussian function and the order of B-splines that approximate it $\sigma = \sqrt{\frac{p+1}{12}}$ [25], the assumption that a Gaussian object is visible approximately over $\pm\sigma$ pixels [15], and the fact that the mammograms in the University of Florida database were digitized at 116μm resolution, four levels of the transform from Section 2.2 with, for example, $p=3$ are needed to encompass different sizes of microcalcifications. The wavelet decomposition including voices at scales 3 and 6 (corresponding to Strickland and Hahn's octaves "2.5" and "3.5") can be obtained by deriving a counterpart to Equation (18) for the two scales.
$\hat{\beta}_p(3\omega)$ can be related to $\hat{\beta}_p(\omega)$ by expressing $\hat{\beta}_p(3\omega)$ as (cf. Proposition 1 of [26])

$$\hat{\beta}_p(3\omega) = \frac{1}{3^{p+1}} \left(\frac{\sin\left(\frac{3\omega}{2}\right)}{\sin\left(\frac{\omega}{2}\right)} \right)^{p+1} \left(\frac{\sin\left(\frac{\omega}{2}\right)}{\frac{\omega}{2}} \right)^{p+1}.$$

Using $\sum_{m=0}^{M} e^{j(m\omega+\theta)} = \frac{\sin\left(\frac{(M+1)\omega}{2}\right)}{\sin\left(\frac{\omega}{2}\right)} e^{j\left(\frac{M\omega}{2}+\theta\right)}$, we get

$$\hat{\beta}_p(3\omega) = V(\omega)\hat{\beta}_p(\omega),$$

where

$$V(\omega) = \left(\frac{1}{3}\left(e^{-j\omega} + 1 + e^{j\omega}\right) \right)^{p+1}.$$

Filter $V(\omega)$ can be implemented as a moving sum with $2(p+1)$ additions per sample and a multiplicative factor $\frac{1}{3^{p+1}}$ applied to the wavelet coefficients [26].
Next, $\hat{\beta}_p(6\omega)$ is expressed by means of Equation (17):

$$\hat{\beta}_p(6\omega) = H_{-s}(3\omega)\hat{\beta}_p(3\omega)$$

with odd orders p used for the sampling shift s to be zero.
Now, we can write

$$\begin{aligned}\mathcal{F}\{W_3^i s(x,y)\big|_{x=n_x,y=n_y}\} \simeq S(\omega_x,\omega_y)\, B_r^{-1}(\omega_x)\, B_r^{-1}(\omega_y)\, B_{p+r+i+1}(\omega_x)\cdot \\ \cdot B_{p+r+d-i+1}(\omega_y)\, G_{-s}^{d-i}(3\omega_x)\, G_{-s}^{i}(3\omega_y) V^{p+i}(\omega_x) V^{p+d-i}(\omega_y) \qquad (35)\end{aligned}$$

and

$$\mathcal{F}\{W_6^i s(x,y)\Big|_{x=n_x,y=n_y}\} \simeq S(\omega_x,\omega_y)\, B_r^{-1}(\omega_x)\, B_r^{-1}(\omega_y)\, B_{p+r+i+1}(\omega_x)\cdot$$
$$\cdot B_{p+r+d-i+1}(\omega_y)\, G_{-s}^{d-i}(6\omega_x)\, G_{-s}^{i}(6\omega_y) H_{-s}^{p+i}(3\omega_x) H_{-s}^{p+d-i}(3\omega_y) V^{p+i}(\omega_x) V^{p+d-i}(\omega_y) \qquad (36)$$

with notation being the same as in Equation (18), and superscript p in $H_{-s}^{p}(\omega)$ denoting the order p in Equation (16).

Wavelet coefficients obtained via Equations (35) and (36) are not used for reconstruction—the inverse transform is carried out as given in Section 2.2.

The decomposition described by Equations (18), (35), and (36) with additional filtering by $G^2(l\omega)$ at each scale $l \in \{1,2,3,4,6,8\}$ enables approximations to the second derivatives of Gaussian along both x and y directions and to Laplacian of Gaussian across distinct scales employed by Strickland and Hahn [15] (cf. Equations (33) and (34)). We proceed in a similar fashion as therein: the two outputs per scale are thresholded independently, all binary results are then combined, a circular region centered at detected pixel locations are next multiplied by a gain, and, finally, the reconstruction process uses modified transform coefficients.

2.3.2 Circumscribed Masses

Almost half of missed cancers appear on mammograms as masses. Perception is a problem particularly for patients with dense fibroglandular patterns. The detection of masses can be especially difficult because of their small size and subtle contrast compared with normal breast structures.

Fan and Laine [10] developed a discrete dyadic wavelet transform based algorithm suitable for enhancement of masses. They constructed an approximation to Laplacian of Gaussian across dyadic scales for an isotropic input to a piecewise linear enhancement function. Approximation to Laplacian of Gaussian across dyadic scales is easy to obtain using multiscale spline derivatives derived in Section 2.2: Equation (18) with $i=0$ and $i=2$ approximates the second derivative of a Gaussian function along directions of x and y axis, respectively (the corresponding branches in Figure 2(c) are the first and third from the top). The appropriate transform coefficient at each dyadic scales are therefore added and their sum input to the piecewise linear function

$$C(x) = \begin{cases} x - (K-1)T & \text{if } x < -T \\ Kx & \text{if } |x| \le T \\ x + (K-1)T & \text{if } x > T. \end{cases} \qquad (37)$$

used at each level $m+1$ of the transform separately. Due to the expected size of masses, levels greater than 4 are enhanced more aggressively.

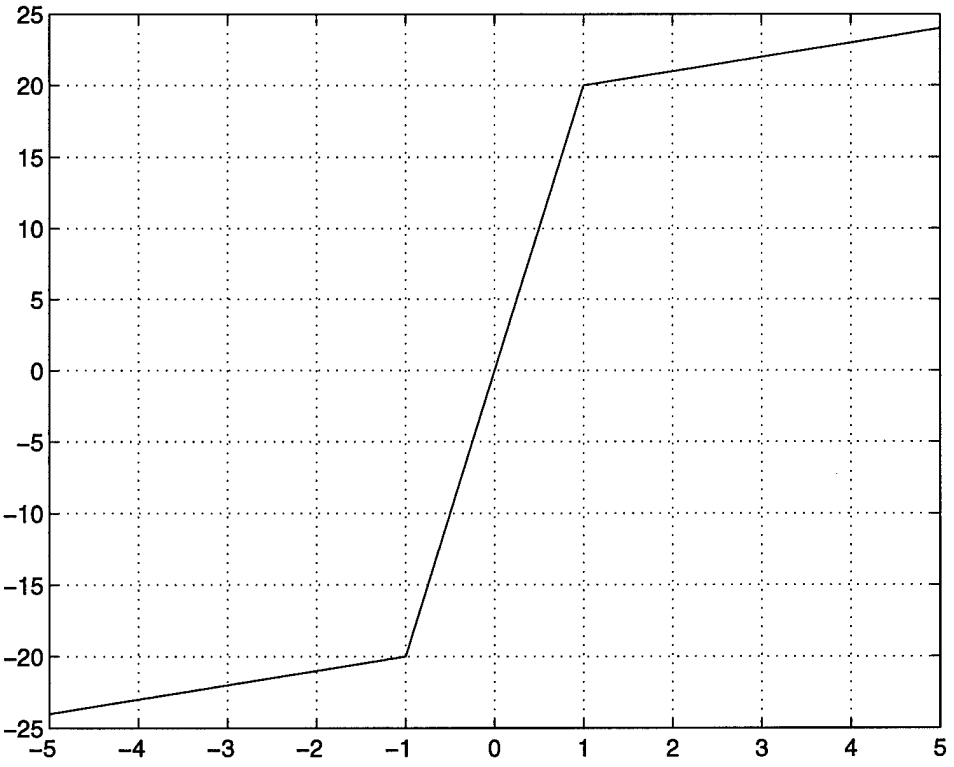

Figure 4: Enhancement function (Equation (37) with $K = 20$ and $T = 1$).

Figure 4 shows the enhancement function from Equation (37) for parameter values $K = 20$ and $T = 1$.

The multiplicative factor obtained as the ratio between the output and input of the enhancement function is next applied to the original wavelet coefficients [10], and then the reconstruction (Figure 2(b) and (d)) is carried out.

Figure 5 shows the cranio-caudal view of a patient with bloody nipple discharge. On the enhanced image cropped to the area of interest, irregular anterior borders of a mass are better seen.

2.3.3 Stellate Lesions

It is important for radiologists to identify stellate lesions since their presence is a serious indicator of malignancy. Stellate lesions vary in size and subtlety and, in addition, do not have a clear boundary, making them difficult to detect.

In the development of our algorithm, we follow an observation made by Kegelmeyer *et al.* about the distortion of edge orientation distribution induced by a stellate lesion [27]. Normal mammograms show a roughly radial pattern with structure radiating from the nipple to the chest wall. A stellate lesion not only changes this pattern, but also creates

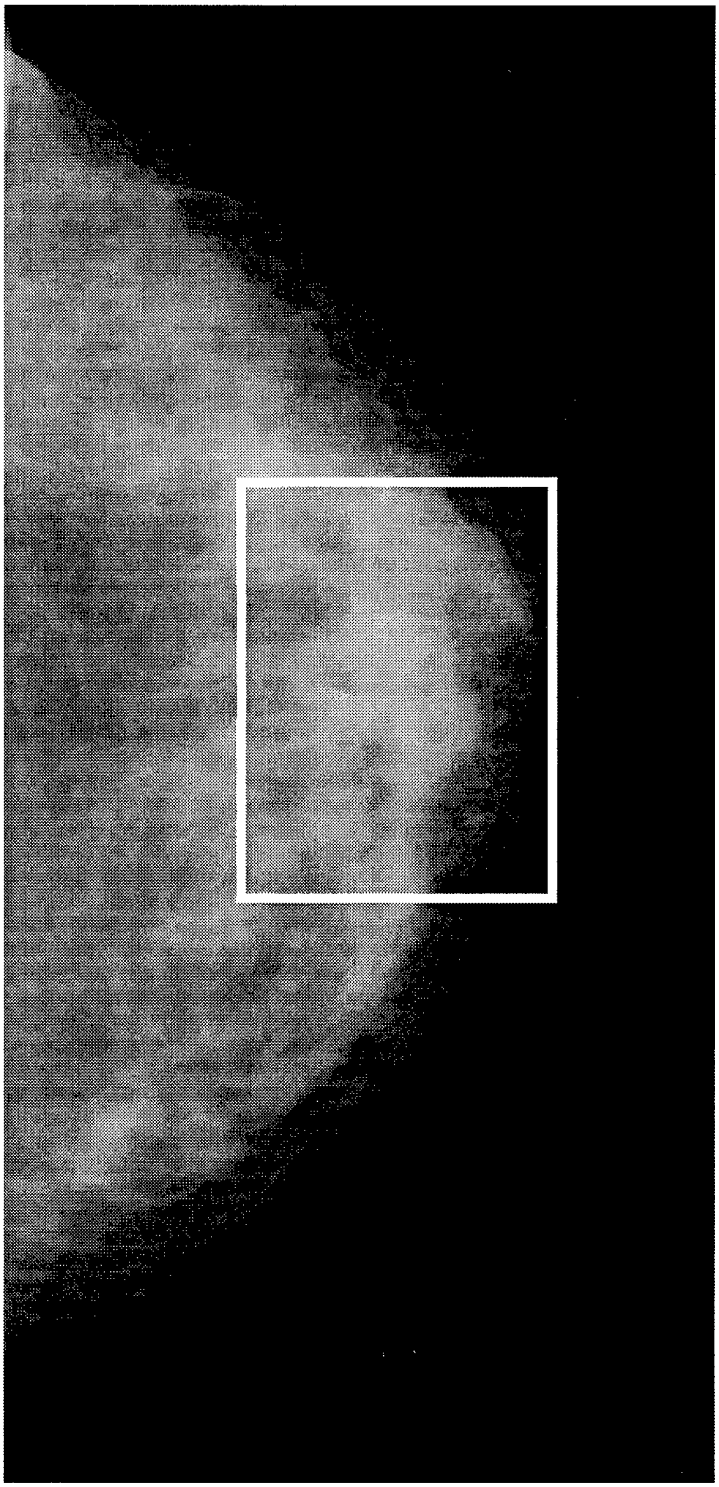

(a)

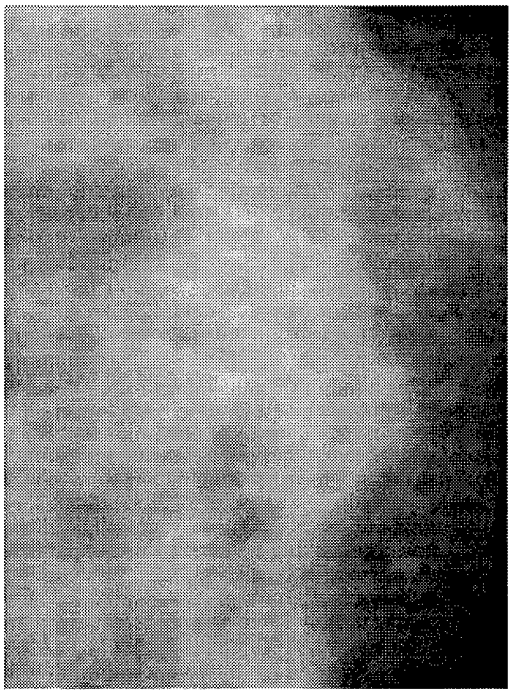

(b)

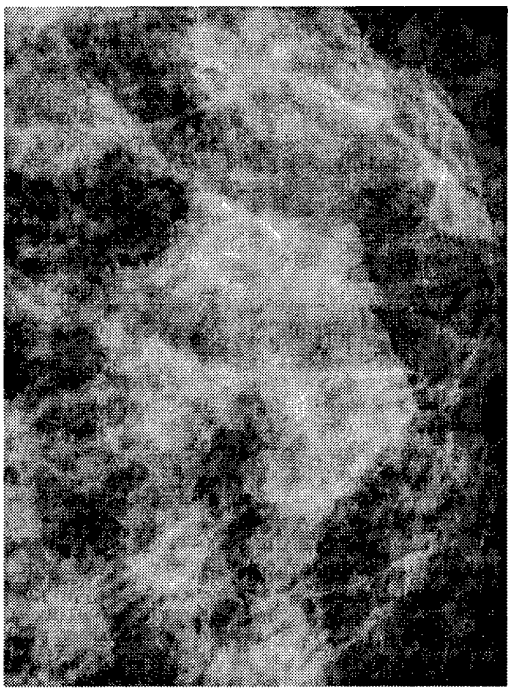

(c)

Figure 5: Contrast enhancement of the cranio-caudal of a patient with bloody nipple discharge. (a) The original mammogram with area of interest delineated. (b) Unprocessed extracted area. (c) The enhanced area improves the visualization of the mass.

another center from which rays radiate. Directional analysis using the Sobel edge operator was employed for assessment of local orientations [27].

Wavelet transform from Section 2.2 enables directional analysis as well. By adding additional filter $G^1_{-s}(2^m\omega)$ to each scale of decomposition from Figure 2, approximations to both first and second steerable derivatives of a Gaussian are available. A multiscale derivative-pair quadratic feature detector is computed by finding the maximum of the local oriented energy with respect to angle θ

$$E^{\theta}_{2^m}(x,y) = \sqrt{(W1^{\theta}_{2^m}s(x,y))^2 + (W2^{\theta}_{2^m}s(x,y))^2}, \tag{38}$$

where $W1^{\theta}_{2^m}s(x,y)$ and $W2^{\theta}_{2^m}s(x,y)$ denote wavelet decompositions using first (Equation (6) with $d=1$) and second (Equation (6) with $d=2$) derivative wavelet, respectively, steered to angle θ. The angle that maximizes the local oriented energy (38) represents orientation at pixel location (x,y).

Similarly to the method from Section 2.3.1, processing is carried out within windows with scale dependent sizes: 1-norm of differences between the local and average orientations is computed in the window and used as a measure of orientation nonuniformity. Soft thresholding as a function of the orientation nonuniformity measure is next applied to the transform coefficients at each dyadic scale independently [9]. The altered coefficients are then included for reconstruction.

Figure 6 shows the oblique view with a mass visible in the mid-posterior breast. The enhanced image demonstrates the irregularity and spiculation of the mass.

2.4 Fusion of Enhanced Features

Enhanced features from Section 2.3 are fused into the final enhanced image. Image fusion using redundant steerable wavelet representations was treated in detail in our previous report, so let us only point out that the fusion used here is implicit rather than explicit: wavelet transform coefficients are first modified for enhancement of microcalcifications, circumscribed masses, and stellate lesions, and then the new coefficients are obtained by fusion before the reconstruction is accomplished.

Note also that it is possible to put different weights on features, and exclude certain features from the final result.

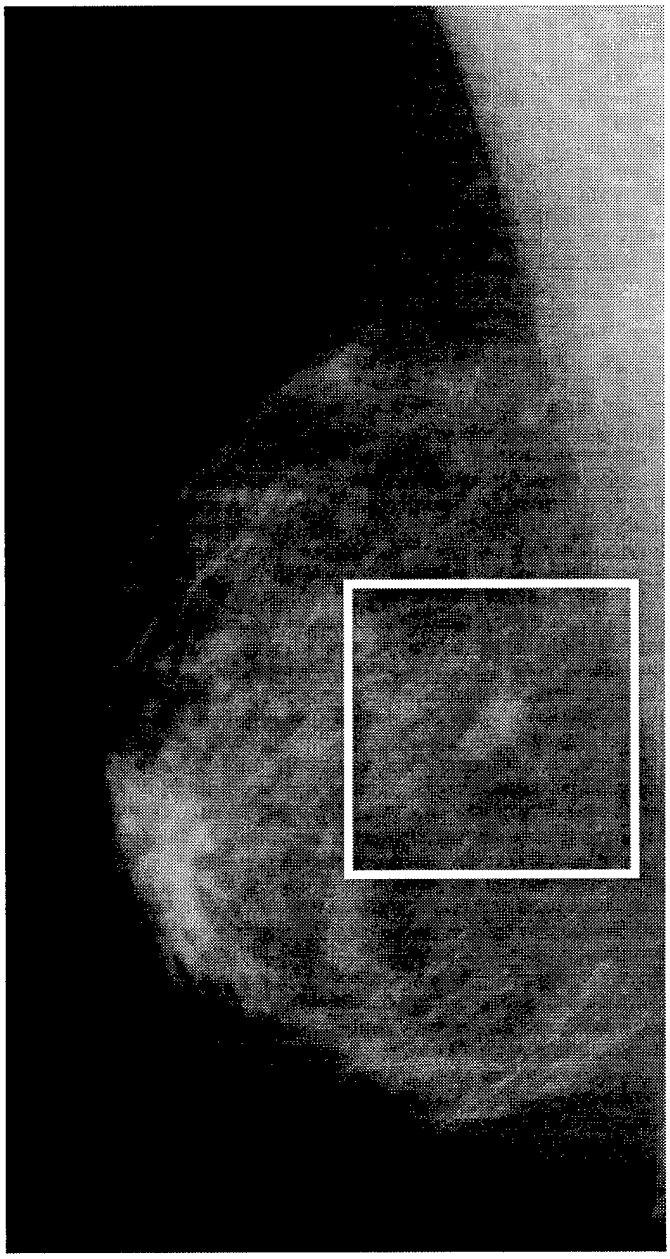

(a)

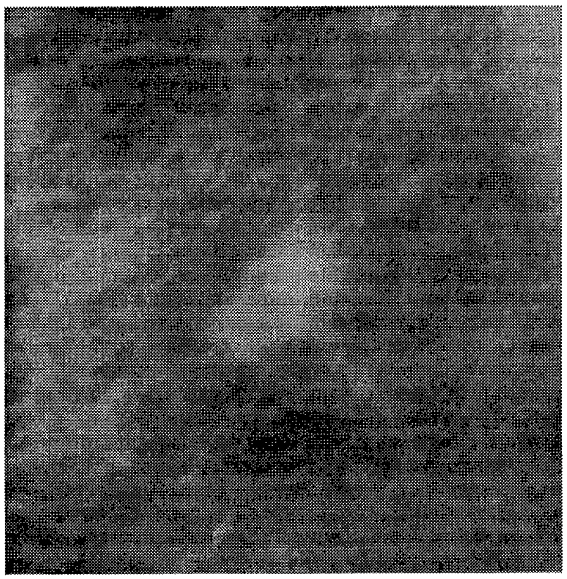

(b)

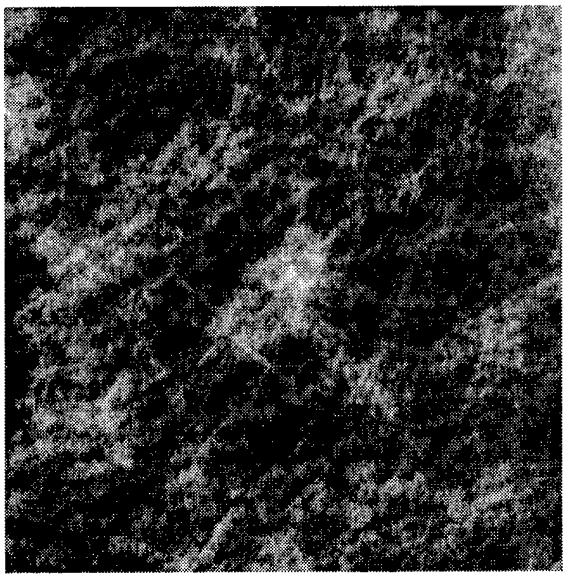

(c)

Figure 6: Contrast enhancement of the oblique view. (a) The original mammogram with area of interest delineated. (b) Unprocessed extracted area. (c) The enhanced area improves the visibility of the mass.

3 Conclusions

During our second year, we developed a method that improves the visibility of specific mammographic features by local enhancement and fusion of the enhanced areas. The described method incorporates a variety of properties of mammographic image enhancement methods tailored to specific signs of malignancy into a unified computational framework.

We derived a wavelet transform with analysis stage enabling approximations to directional first and second derivatives of a Gaussian function and to Laplacian of Gaussian across distinct scales. Such a decomposition is suitable for both anisotropic and isotropic multiscale analysis, and, in addition, provides an adaptable framework for incorporation of a variety of mammographic processing methods.

The derived transform has also proved flexible enough for enhancement and fusion of individual types of mammographic features. Separate enhancement algorithms have been developed for microcalcifications, circumscribed masses, and stellate lesions, and fusion of the modified transform coefficients performed before the reconstruction of the final enhanced image. It is worth mentioning that there is a certain overlap between the enhancement modules: for example, the enhancement strategy developed for stellate lesions may also enhance circumscribed masses and vice versa since the two share many common properties.

In addition to its efficiency, the algorithm is also well suited for further refinements; optimizations can be performed for each type of malignancy alone, and separately for the fusion module.

The work in the final year of our investigation will concentrate on extensive testing and possible refinements of the developed algorithms.

References

[1] S. L. Parker, T. Tong, S. Bolden, and P. A. Wingo, "Cancer statistics 1996," *CA–A Cancer Journal for Clinicians*, vol. 46, no. 1, pp. 5–27, 1996.

[2] R. A. Smith, "Epidemiology of breast cancer," in *A Categorical Course in Physics, Technical Aspects of Breast Imaging*, A. G. Haus and M. J. Yaffe, Eds. The 79th Scientific Assembly and Annual Meeting of the Radiological Society of North America (RSNA), 1993, pp. 21–33.

[3] P. C. Johns and M. J. Yaffe, "X-ray characterization of normal and neoplastic breast tissues," *Physics in Medicine and Biology*, vol. 32, no. 6, pp. 675–695, 1987.

[4] M. J. Yaffe, R. J. Jennings, R. Fahrig, and T. R. Fewell, "X-ray spectral considerations for mammography," in *A Categorical Course in Physics, Technical Aspects of Breast Imaging*, A. G. Haus and M. J. Yaffe, Eds. The 79th Scientific Assembly and Annual Meeting of the Radiological Society of North America (RSNA), 1993, pp. 63–72.

[5] A. F. Laine, S. Schuler, J. Fan, and W. Huda, "Mammographic feature enhancement by multiscale analysis," *IEEE Trans. Med. Imaging*, vol. 13, no. 4, pp. 725–740, 1994.

[6] A. Laine, W. Huda, B. G. Steinbach, and J. C. Honeyman, "Mammographic image processing using wavelet processing techniques," *Eur. Radiology*, vol. 5, pp. 518–523, 1995.

[7] A. Laine, J. Fan, and W. Yang, "Wavelets for contrast enhancement of digital mammography," *IEEE Eng. Med. Biol. Mag.*, vol. 14, no. 5, pp. 536–550, 1995.

[8] A. Laine, J. Fan, and S. Schuler, "A framework for contrast enhancement by dyadic wavelet analysis," in *Digital Mammography*, A. G. Gale, S. M. Astley, D. R. Dance, and A. Y. Cairns, Eds., Elsevier, Amsterdam, The Netherlands, 1994, pp. 91–100.

[9] I. Koren, A. Laine, F. Taylor, and M. Lewis, "Interactive wavelet processing and techniques applied to digital mammography," in *Proc. IEEE Int. Conf. Acoust. Speech Signal Process.*, Atlanta, GA, 1996, vol. 3, pp. 1415–1418.

[10] J. Fan and A. Laine, "Multiscale contrast enhancement and denoising in digital radiographs," in *Wavelets in Medicine and Biology*, A. Aldroubi and M. Unser, Eds., CRC Press, Boca Raton, FL, 1996, pp. 163–189.

[11] S. Mallat and S. Zhong, "Characterization of signals from multiscale edges," *IEEE Trans. Pattern Anal. Mach. Intell.*, vol. 14, no. 7, pp. 710–732, 1992.

[12] I. Koren and A. Laine, "A discrete dyadic wavelet transform for multidimensional feature analysis," in *Time-Frequency and Wavelets in Biomedical Signal Engineering*, M. Akay, Ed., IEEE Press, New York, NY, 1997, pp. 425–449.

[13] C.-M. Chang and A. Laine, "Enhancement of mammograms from oriented information," in *Proc. IEEE Int. Conf. Image Process.*, Santa Barbara, CA, 1997, vol. 3, pp. 524–527.

[14] W. M. Morrow, R. B. Paranjape, R. M. Rangayyan, and J. E. L. Desautels, "Region-based contrast enhancement of mammograms," *IEEE Trans. Med. Imaging*, vol. 11, no. 3, pp. 392–406, 1992.

[15] R. N. Strickland and H. I. Hahn, "Wavelet transforms for detecting microcalcifications in mammograms," *IEEE Trans. Med. Imaging*, vol. 15, no. 2, pp. 218–229, 1996.

[16] H. Yoshida, W. Zhang, W. Cai, K. Doi, R. M. Nishikawa, and M. L. Giger, "Optimizing wavelet transform based on supervised learning for detection of microcalcifications in digital mammograms," in *Proc. IEEE Int. Conf. Image Process.*, 1995, vol. 3.

[17] I. Koren, A. Laine, and F. Taylor, "Image fusion using steerable dyadic wavelet transform," in *Proc. IEEE Int. Conf. Image Process.*, Washington, D.C., 1995, vol. 3, pp. 232–235.

[18] I. Koren, *A multiscale spline derivative-based transform for image fusion and enhancement*, PhD thesis, Department of Electrical and Computer Engineering, University of Florida, Gainesville, FL, 1996.

[19] A. J. Jerri, "The Shannon sampling theorem—its various extensions and applications: A tutorial review," *Proc. IEEE*, vol. 65, no. 11, pp. 1565–1596, 1977.

[20] A. V. Oppenheim and R. W. Schafer, *Discrete-Time Signal Processing*, Prentice-Hall, Englewood Cliffs, NJ, 1989.

[21] O. Rioul and P. Duhamel, "Fast algorithms for discrete and continuous wavelet transforms," *IEEE Trans. Inf. Theory*, vol. 38, no. 2, pp. 569–586, 1992.

[22] M. Unser, A. Aldroubi, and M. Eden, "Fast B-spline transforms for continuous image representation and interpolation," *IEEE Trans. Pattern Anal. Mach. Intell.*, vol. 13, no. 3, pp. 277–285, 1991.

[23] L. W. Estevez and N. D. Kehtarnavaz, "Computer assisted enhancement of mammograms for detection of microcalcifications," in *Proc. IEEE Symp. Comput. Based Med. Syst.*, 1995, pp. 16–23.

[24] H. Li, K. J. R. Liu, and S. C. B. Lo, "Fractal modeling of mammogram and enhancement of microcalcifications," in *Proc. IEEE Nucl. Sci. Symp. Med. Imaging Conf.*, 1997, vol. 3, pp. 1850–1854.

[25] M. Unser, A. Aldroubi, and M. Eden, "On the asymptotic convergence of B-spline wavelets to Gabor functions," *IEEE Trans. Inf. Theory*, vol. 38, no. 2, pp. 864–872, 1992.

[26] M. Unser, A. Aldroubi, and S. J. Schiff, "Fast implementation of the continuous wavelet transform with integer scales," *IEEE Trans. Signal Process.*, vol. 42, no. 12, pp. 3519–3523, 1994.

[27] W. P. Kegelmeyer, J. M. Pruneda, P. D. Bourland, A. Hillis, M. V. Riggs, and M. L. Nipper, "Computer-aided mammographic screening for spiculated lesions," *Radiology*, vol. 191, no. 2, pp. 331–337, 1994.